Attachment and Solvation of the H^- Dopant: Structures of Ne_nH^- and Ar_nH^- Clusters from Energy-Optimizing Calculations†

F. Sebastianelli and F. A. Gianturco*

Department of Chemistry, University of Rome "La Sapienza", P.le Aldo Moro 5, 00185 Roma, Italy

Received: February 20, 2004; In Final Form: April 14, 2004

The structural properties and the energetics of clusters of argon and neon atoms containing the atomic impurity H^-, Ne_nH^-, and Ar_nH^-, with n varying from 9 up to 25, are examined. The same calculations are also carried out for the corresponding neutral homogeneous clusters, Ne_n and Ar_n. The results of the calculations, the physical reliability of the present modeling of the interactions, and the similarities, as well as the differences, between the anionic and the neutral complexes are discussed in some detail. The emerging picture shows that the dopant atom H^- always locates itself outside the Ne_n moiety without significantly affecting the overall geometry of the cluster, while on the other hand, the Ar_nH^- and Ar_{n+1} clusters present very similar structures in which the H^- dopant replaces one of the inner Ar atoms and therefore becomes fully "solvated" within the cluster.

I. Introduction

The interest in small ionic clusters involving rare gas (Rg) atoms has markedly increased over the years from both the theoretical and the experimental viewpoints.[1−6] In the experimental[7,8] and the theoretical[9−16] views, the positively charged argon clusters $(Ar_n)^+$ and the corresponding protonated aggregates $(Ar_nH)^+$ are known to consist of an arrangement of neutral, or almost neutral, Ar atoms, which are bound by polarization forces and, to a lesser degree, by dispersion forces to a moiety over which the majority of the charge resides, $[Ar_k]^+$ or $[Ar_{k'}H]^+$ with k (k') ranging from 2 to 4 (1 to 2), depending on the cluster size and on the method employed to characterize them. Analogous results have been obtained for the $(Ne_n)^+$ clusters, for which the theoretical[17−21] and the experimental[22−25] data converge in defining as the charged core the dimeric unit $[Ne_2]^+$: they all show, however, very different structural features with respect to the neutral Ar_n and Ne_n clusters because the interaction potential between the ionic core and the other Rg atoms is usually more than 3 orders of magnitude greater than that between argon or neon atoms in the neutral aggregates. Indeed, for cationic clusters, a stable molecular species is usually formed inside the cluster.[12] On the other hand, a behavior more similar to that of the neutral aggregates is shown by argon and neon clusters in the presence of an anionic impurity $(Rg)_nY^-$ (where Y stands both for atomic and molecular species). As compared to these, the positive charge is more delocalized and both experimental[26−29] and theoretical[27,28,30−32] evidence concurs in indicating that the excess negative charge is largely preserved on the Y^- subion, the latter being not much structurally perturbed with respect to the isolated species. These aggregates are of particular interest because, as we shall see below, much weaker forces are at play; therefore, such complexes are governed by comparable strength of interactions between the "solute" with the "solvent" atoms and the latter units among themselves. This is also what usually occurs in chemical species undergoing solvation in a macroscopic solution; therefore, their study offers a realistic, but simpler, analogy that can help us to gain insight into anionic solvation at the molecular level.[1] The likelihood for anionic solvation to occur is strongly influenced at the microscopic level by the interaction between the negative ion, Y^-, and the first few solvent species surrounding it.

In two of our previous papers, we studied the structure and the energetics of the smaller $(Ne)_nH^-$ and $(Ar)_nH^-$ clusters,[31,32] with n up to 8, making use of high accuracy potential energy curves (PECs) for the $Rg-H^-$ anion interactions.[33] We used both classical and quantum methods and found that the H^- impurity, owing to the specific features of the two-body potentials employed, always locates itself outside the Rg cluster and, therefore, has no tendency to solvate the anionic species, at least for clusters of the size that we considered there. We also examined the lowest energy structures for the corresponding homogeneous neutral counterparts, i.e., $(Ne)_n$ and $(Ar)_{n+1}$, to compare and contrast the anionic clusters and their corresponding neutral species. The overall picture obtained for those systems was as follows.[31,32]

(i) In the ab initio calculations (MP2 with a AUG-cc-pVTZ basis set) that we carried out there, the many-body (MB) contributions affect the final energy only by a small percentage and hardly affect the final geometries, even when looking at the $(Ar)_nH^-$complexes, so that it becomes physically reliable to model the global interaction forces within each cluster as a sum of pairwise potentials.

(ii) Within the pairwise potential model, we estimated the quantum effects on nuclear motion by means of diffusion Monte Carlo (DMC) and distributed Gaussian functions (DGF) calculations in order to make a comparison with the classical, lowest energy structures: even if we found appreciable zero point energy values for all of the clusters, we could also show that the nuclear ground state wave functions of these systems were delocalized about maximum density values corresponding to distances very close to their classically optimized geometries.

(iii) From both the quantum and the classical calculations, we found that in the neon clusters, the dopant atom H^- always locates itself outside the $(Ne)_n$ moiety without significantly

† Part of the "Gert D. Billing Memorial Issue".

* To whom correspondence should be addressed. Fax: +39-06-49913305. E-mail: fa.gianturco@caspur.it.

10.1021/jp0492164 CCC: $27.50
Published on Web 05/18/2004

affecting the overall geometry, while in the argon aggregates, the H^- impurity in the anionic clusters $(Ar)_{n-1}H^-$ locates itself in such a way as to exactly replace one of the outer Ar atoms at its location in the neutral counterpart complex, $(Ar)_n$.

Given these facts, in the present work, we intend to focus our attention on larger $(Ne)_nH^-$ and $(Ar)_nH^-$ clusters, with $9 \leq n \leq 25$, using again the pairwise potential model to describe the global interaction forces and a classical method for the energy-optimizing calculations, to verify whether the H^- dopant undergoes solvation into these clusters or still remains outside the core. We will also look at the corresponding neutral, homogeneous species $(Ne)_n$ and $(Ar)_n$ in order to check the similarities and the different features that appear when a negative ion impurity is inserted into a neutral neon/argon cluster. This could help one to obtain a clearer picture for the relative atomic locations and the distributions of the net charges among the Ne/Ar complexes and the H^- species by looking at the positioning of the H^- impurity with respect to the Ne_n/Ar_{n+1} moiety.

The following section describes the interaction potentials for the anionic species and for the neutral dimers, while in section III we describe the procedure for the calculation of the lowest energy structures of the anionic and the neutral clusters. We present our results in section IV while the last section summarizes our conclusions.

II. The Interaction Forces

The initial quantities that we need to know are the interaction potentials for the diatomic systems Ne_2, Ar_2, NeH^-, and ArH^-. For Ar_2, we use the PEC calculations based on the Tang−Toennies (TT) model,[34] which requires five parameters: the first three are the leading dispersion coefficients, C_{2n}, while two more parameters, A and b, describe the repulsive potential according to the following formula[35]

$$V_{TT}(R) = Ae^{-bR} - \sum_{n=3}^{5} f_{2n}(bR)\frac{C_{2n}}{R^{2n}} \qquad (1)$$

where f_{2n} is the damping function. The equilibrium distance and the well depth so obtained are in excellent agreement with the highly accurate ab initio calculations of ref 36 and with the earlier semiempirical results of Aziz.[37] The Ne_2 ground state potential has been calculated with the CCSD(T) method, carried out using a 240 orbital expansion within an optimized basis set (IO240), which contains a 3s3p2d1f1g set of mid-bond functions.[38] This potential is in good agreement with the very recent experimental one[39] obtained from the map of the rovibrational energy levels of the ground state and determined from high-resolution spectroscopic measurements of the $\Pi\ 0_u^+ \leftarrow X\ 0_g^+$ transition in a vacuum ultraviolet around 16.8 eV. The ArH^- and NeH^- PECs have already been computed at the CCSD(T) level using basis sets containing 167 and 143 orbitals, respectively, and the calculations were carried out with all of the electrons being correlated within the expansion.[33] In Figure 1, we sketch all interaction potentials: as one can immediately see, they show very different features. In fact, in the neon case (see left panel of Figure 1), the Ne−Ne well depth differs by less than 10% from the Ne−H^- one, the neutral dimer being more stable (−28.51 and −26.36 cm^{-1}, respectively), while the equilibrium distances differ by about 2.8 au, with the Ne−H^- minimum reached at 8.7 au and the Ne−Ne one at 5.86 au. On the other hand, in the argon case (see right panel of Figure 1), the Ar−H^- potential is more than 2.7 times that of the neutral system (−272.97 and −99.75 cm^{-1}, respectively), but the

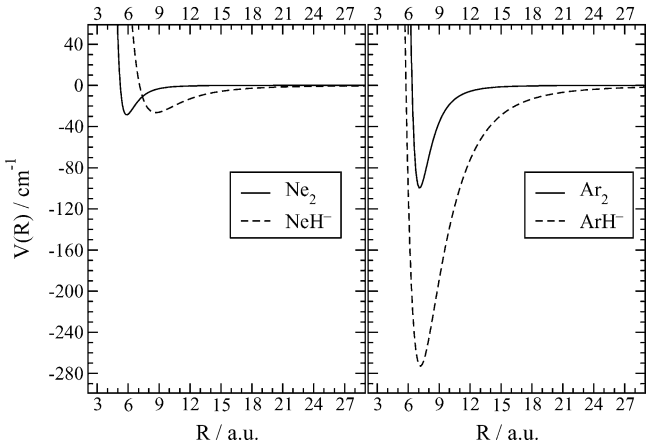

Figure 1. Left panel: ground state PECs for Ne_2 (solid line) calculated in ref 38 and NeH^- (dashed line) calculated in ref 33. Right panel: ground state PECs for Ar_2 (solid line) calculated in ref 35 and ArH^- (dashed line) calculated in ref 33. The energies are in cm^{-1}, and the R values are in a.u.

equilibrium distances, at around 7.1 au, are practically the same. The potential wells of ArH^- and NeH^- are mainly caused by the dipole moment induced on the Ar and Ne atoms by the H^- ion. This charge-induced dipole interaction has an R^{-4} long-range behavior. The long-distance interaction of this system therefore goes to zero much more slowly than the usual dispersion forces that vanish as R^{-6} and which characterize the long-range features of the Ar_2 and Ne_2 curves. Indeed, we can note from that figure, comparing the left with the right panel, that both curves for the neutral dimers become negligible after 12 au, while the ArH^- potential keeps nonnegligible values over a consistently broader range of interatomic distances with respect to the NeH^- interaction. It is this interaction that will also shape the minimum energy region of the curves since it is directly proportional to the Rg atomic polarizability: this explains the much greater value of the well depth for ArH^- with respect to NeH^-, the polarizabilities of Ar and Ne being 11.08 and 2.669 au,[40] respectively.

Standard ab initio methods quickly reach the limit of their applicability with clusters containing only a smallish number of atoms. Various alternative techniques have therefore been devised in order to have realistic, but easier to achieve, descriptions of the interaction forces. Given the great difference between the electron affinity of H (72.77 kJ mol^{-1}, as reported in ref 41) and Ne and Ar atoms (−29 and −35 kJ mol^{-1}, respectively[42]), we can guess that in the Rg_nH^- clusters the negative charge will reside essentially on the H atom; hence, we could make the assumption that the global interaction potential in those systems should be correctly described by just a sum of pairwise potentials, neglecting the MB effects, as we verified in refs 31 and 32 for the smaller clusters (n up to 8). This means that we can approximate the full set of forces as the individual interactions between H^- and the relevant number of Rg atoms. Thus, for a generic Rg_nH^-, cluster we can write

$$V_{TOT} = \sum_{i=1}^{n} V^i_{(Rg-H)^-} + \sum_{\substack{i,j=1 \\ i<j}}^{n} V^{ij}_{(Rg-Rg)} \qquad (2)$$

in which the first term is the sum of the interactions in the RgH^- systems for which we employed the calculations of ref 33, and the second term is the sum of the interactions between two neutral Rg atoms for which we used the results of refs 35 and 38. We shall also employ the same modeling of interaction

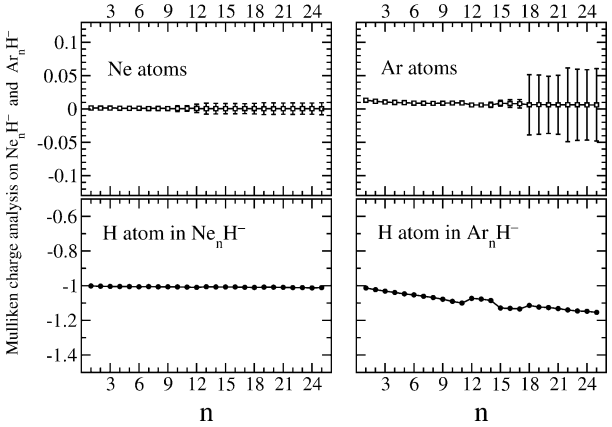

Figure 2. Left panel: Mulliken charge analysis for the Ne_nH^- clusters. Right panel: Mulliken charge analysis for the Ar_nH^- clusters. In the lower part of each panel, the fraction of the charge on the H atom is shown for each complex with n up to 25. In the upper part of each panel, the average values of the fraction of the charge on the Rg atoms are reported along with their statistical standard deviation. The charge analysis is carried out on the geometries of the lowest energy structures optimized using pairwise potentials and classical optimization.

forces to describe the corresponding neutral, homogeneous Rg_n clusters, i.e., we shall write:

$$V_{\mathrm{TOT}}^{\mathrm{neutral}} = \sum_{\substack{i,j=1 \\ i<j}}^{n} V_{(\mathrm{Rg-Rg})}^{ij} \tag{3}$$

Their analysis and comparison will be given below, along with our discussion for the anionic clusters. With the modeling of V_{TOT} as in eqs 2 and 3, we are neglecting the MB interaction terms. While for the neutral aggregates this approximation is known to give a fairly good description of the systems,[43] more attention has to be paid when looking at the larger aggregates. To probe the physical reliability of choice (2) to describe anionic clusters, we carried out the Mulliken charge analysis on the geometries of the optimized lowest energy structures for the Rg_nH^- clusters (which will be discussed in detail in section IV) that were obtained first by using the pairwise potential model and the classical optimization described in section III. Our calculations of their charge distributions were obtained with the GAUSSIAN 98 program package,[44] as reported in Figure 2.

In the left panel of that figure, the analysis for the Ne_nH^- aggregates shows that the negative charge resides completely on the H atom (lower graph) and that even for the larger values of n, the Ne atoms remain, on the average, neutral (see the standard deviations in the upper graph). The same Mulliken analysis is made for the Ar complexes (see the right panel of Figure 2), where we report the mean values of the fraction of the charge on the different atoms along with their statistical standard deviations as a function of the cluster size n. Also in this case, one can see that the negative charge is practically localized only on the H atom, the argon atoms remaining, on the average, almost neutral, even if the standard deviations (upper part of the right panel of Figure 2) show a small delocalization of the negative charge among Ar atoms, in contrast with the Ne_nH^- case. However, the fraction of negative charge on the Ar atoms is so small that the present results confirm the reliability of our assumption to model the global forces within each anionic cluster as a sum of pairwise potentials (eqs 2 and 3). These findings are also in line with the results of refs 27 and 28 for the Ar_nY^- clusters, where $Y = Cl^-, Br^-, I^-$. These authors carried out simulated annealing molecular dynamics calculations, which included the effects of the MB terms and found structures similar to those that we obtained for Ar_nH^-. They also confirmed that the MB terms are more important for getting good agreement with experimental values that involve electronic structure properties such as the electron affinity, rather than affecting the actual cluster geometries as given by the pairwise potential models. Interestingly enough, these H^--doped Rg clusters give us the opportunity to explore two paradigmatic cases as far as the interaction potential between the constituting diatomic pairs is concerned, as we shall further discuss below.

III. Calculations of Cluster Structures

Having set up all of the necessary interaction potentials, the next task is to employ them for geometry optimization studies. We use cubic splines to fit the $V_{(\mathrm{Rg-H})^-}^{i}$ and $V_{(\mathrm{Rg-Rg})}^{ij}$ terms of eqs 2 and 3 in order to have an analytic representation of V_{TOT} and then write down its first and second derivatives. The total potential in each cluster is described by the sum of pairwise potentials, and searching for the global minimum on this hypersurface will give us the lowest energy structure for each aggregate. All of the classical minimizations were carried out via the OPTIM code[45] implemented by us for our potentials, generating the potential's first and second derivatives in Cartesian coordinates to yield the analytic expressions of its Hessian. The basis of the method is the introduction of an additional Lagrange parameter into the optimization framework that provides simultaneous minimization of all of the dimensions (see ref 46 and references therein). All searches were conducted in Cartesian coordinates using projection operators to remove overall translation and rotation.[47] Analytic first and second derivatives of the energy were used at every step. The energy change corresponding to the optimal step with $h_i = F_i/(\lambda_i - b_i)$ is

$$\Delta E = \sum_i \frac{[\lambda_i - (1/2)b_i]F_i^2}{(\lambda_i - b_i)^2} \tag{4}$$

where the λ_i is the Lagrange multiplier for the i-th degree of freedom, b_i is the i-th Hessian eigenvalue, and F_i is the component of the gradient along the direction of the corresponding Hessian eigenvector. We must now select a λ_i such that $(1/2)b_i - \lambda_i > 0$ for minimization and $(1/2)b_i - \lambda_i < 0$ for maximization, and $\lambda_i \to 0$ for $F_i \to 0$, so that the Newton−Raphson step is recovered near a stationary point. Furthermore, to be sure of having obtained the global minimum for all systems (the number of local minima increases exponentially with the cluster size n), we adopt the following procedure: for each cluster, we use our implementation of the OPTIM code starting with different, randomly generated sets of input coordinates. For each set, we further constrain the initial distances between the Rg and the H^- atoms to vary over a different range of values (i.e., sampling the repulsive, the attractive, and the long-range regions of the interaction) in order to visit most regions of the configurational space of all of the cluster structures under inspection. As an example of our procedure, we show in Figure 3 the energy optimization calculations for $Ar_{18}H^-$, where we report along the x-axis the number of sets of randomly generated input coordinates, which manage to reach an energy minimum geometry (i.e., the Hessian has no negative eigenvalues) and along the y-axis the energy values corresponding to each minimum, so that each point on the curve represents a local minimum. The behavior of this curve as an almost continuous

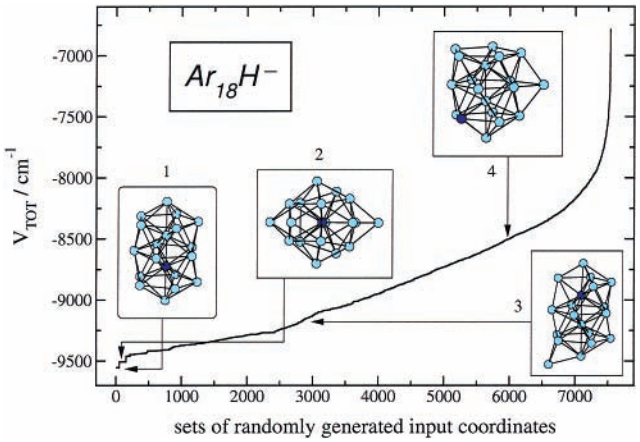

Figure 3. $Ar_{18}H^-$ classical optimization: we report along the *x*-axis the number of input random coordinates yielding a local minimum and along the *y*-coordinates the corresponding values for these energy minima. Also shown are the geometrical structures (numbered from the one giving the lowest energy) associated with some of the energy minima. The energy values are in cm^{-1}.

function indicates the presence of a great number of different local minima, the small stepwise parts of the curve being limited only to relatively stable or symmetrical structures, which the optimization procedure is able to locate easily. We also show in the same figure the geometrical structures (numbered from the one giving the lowest energy) associated with some of the energy minima. When increasing the cluster size, the most relevant problem that we have to face is the exponential growth of the number of local minima with respect to the number of particles inside each cluster. We made several different runs using a different number of sets of initial, randomly generated input coordinates in order to test the reliability of our procedure in finding the overall global minimum on the hypersurface ($\sum V_{Rg-Rg} + \sum V_{Rg-H}$) corresponding to the cluster under inspection. Therefore, for structures of selected size, we carried out calculations using 1500, 6000, and 9000 sets of input coordinates, and we found that for the larger clusters considered, $22 \leq n \leq 25$, a greater value of starting input coordinate sets was needed to get the same lowest energy structure in the different test runs. In a recent paper, Naumkin and Wales[48] found the global potential energy minima for the neutral Ar_n up to $n = 55$, using the Aziz potential[37] and carrying out the optimizations with a basin-hopping method.[49] In Figure 4, we present the comparisons of the energetics and structural features between our results and those of ref 48 for the Ar_n clusters. In the left panel, upper graph, of that figure, we report the total energies of the lowest energy structures that we obtained in comparison with the calculations in ref 48, given by the crosses. To look more in detail at the differences between the two sets of data, in the lower panel, we show the percentage difference, as defined in the formula given there: one can see that this difference is always in the range of $\pm|0.5|$, the value for $n = 2$ indicating the discrepancy between the Ar_2 potential[35] employed in our calculations and the potential from ref 37 used in ref 48. Moreover, if we look at the right panel of Figure 4, where the comparison of the three moments of inertia as a function of the cluster size *n* is shown, we see that the geometrical features of the two sets of data are exactly the same. In fact, we obtained the same series of global minima structures (and belonging to the same point group) as found by Naumkin and Wales,[48,50] also for the Ar_{21} whose global minimum (C_1 symmetry) is the only one that presents a different structure with respect to the corresponding known Lennard−Jones $(LJ)_{21}$ cluster (C_{2v} symmetry). With the basin-hopping method, it was possible to locate successfully all of the known $(LJ)_n$ lowest energy structures up to $n = 110$, including three minima not previously reported.[49] The agreement with the basin-hopping optimizations of ref 48 for the neutral Ar_n makes us confident that our procedure is able to correctly locate all of the global minima (at least for the cluster size considered here) and that we should be able to reach the same level of confidence also for the Rg_nH^- aggregates.

IV. Present Results

As pointed out in section I, the geometrical features and, to a lesser degree, the energy patterns of the smaller (*n* up to 8) complexes obtained by means of the classical optimization method are in line with the quantum description carried out with the DGF and the DMC methods.[31,32] Hence, we can surmise that looking at the lowest energy structures of the larger clusters from classical optimizations can also give us realistic information on the behavior of these aggregates. The study of clusters of increasing size permits us to check the presence of "magic numbers": it is known, in fact, that the appearance of such magic numbers is connected to the presence of particularly stable structures and, in the case of ligand shells around the ion, to the evidence for shell closures. Another question involved in increasing the cluster sizes is the ensuing competition between icosahedral and close-packed geometries.[51] To better discuss this point, let us now see the results of the present calculations. In Figure 5, we show the lowest energy structures (for each geometry, we also report the symmetry group to which it belongs) for some of the Ne_nH^- and the corresponding neutral Ne_n aggregates, sampling the full range of clusters studied here: from left to right, we report the anionic and neutral species with respect to the increasing number *n* of neon atoms, while from top to bottom we report the direct comparison between each Ne_nH^- and Ne_n cluster. First, for the neutral species Ne_n (also occurring for those structures, with *n* from 9 up to 25, not shown in the figure), we find that as for the well-known case of the LJ cluster,[52] the growth sequence is based on the pentagonal bipyramid (the geometry of Ne_7), a very compact structure composed of a ring of five nearly regular tetrahedra, i.e., five atoms form a pentagon and the remaining two are located in the apical positions along the direction perpendicular to that plane. Starting from Ne_8, one neon atom locates itself on each face of the pentagonal bipyramid (see the structure of Ne_{10}) until another five atom ring is formed; for the Ne_{13} cluster, we thus have the highly symmetrical icosahedral geometry. From this structure on, the Mackay icosahedron[53] provides the dominant structural pattern: for the larger clusters, the global minimum is built up with a Mackay icosahedron at the core surrounded by a low-energy overlayer, the Ne_{19} geometry being a double icosahedron; see the lower part of Figure 5. In the upper part of the same figure, we show the lowest energy structures for some of the Ne_nH^- aggregates. The top−bottom arrangement of Ne_nH^- and Ne_n in the various panels is meant to better reveal the effect of the H^- dopant attached on the neutral neon clusters: the negative ion impurity always locates itself outside the Ne_n moiety, which is only slightly perturbed from its neutral structure resembling the geometry of the corresponding isolated neutral counterpart. Similarly to Figure 5, in Figure 6, we report some of the optimized lowest energy structures for Ar_nH^- and Ar_{n+1} (all computed structures, geometries, and energy values are available on request from the corresponding author). For the neutral species, Ar_{n+1}, we find the same growth sequence obtained for the Ne_{n+1} clusters, i.e., each structure is the same as that obtained with the LJ potentials except (as already noted in section III) for $n + 1 =$

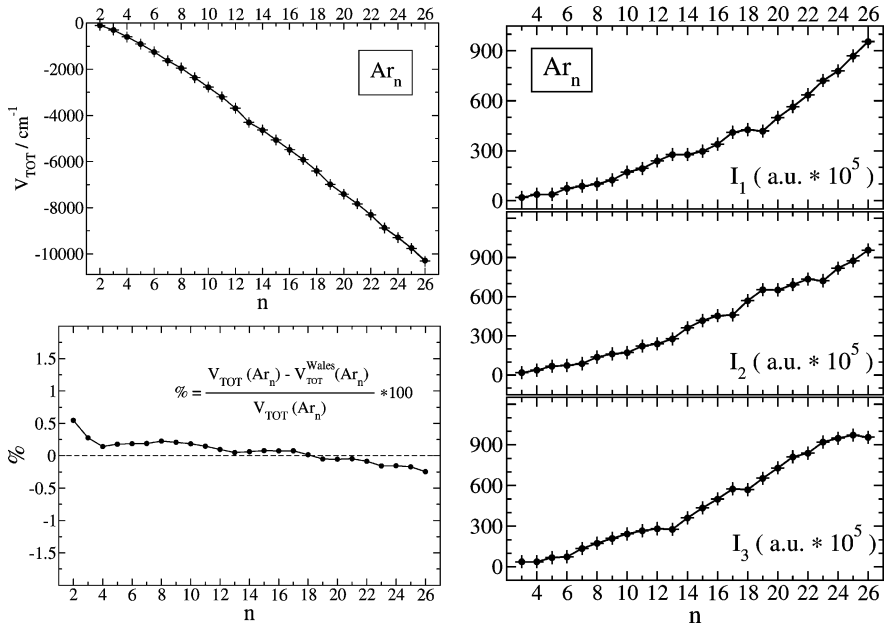

Figure 4. Left panel, upper part: total energies of the lowest energy structures for the Ar_n clusters, as a function of the cluster size n, employing the Ar−Ar potential of ref 35 and the energy-optimizing method described in this section (filled-in circles) in comparison with the results (crosses) of ref 48 employing the Aziz potential.[37] Left panel, lower part: percentage difference, as defined in the formula of the figure, between our calculations and those of ref 48. Right panel: comparison of the three moments of inertia (in units of $a_0 \times 10^5$) as functions of the cluster size n for the Ar_n optimized structures obtained by us (filled-in circles) and those from ref 48 (crosses). The coordinates of the lowest energy structures obtained employing the basin-hopping technique are taken from the Cambridge Cluster Database.[50]

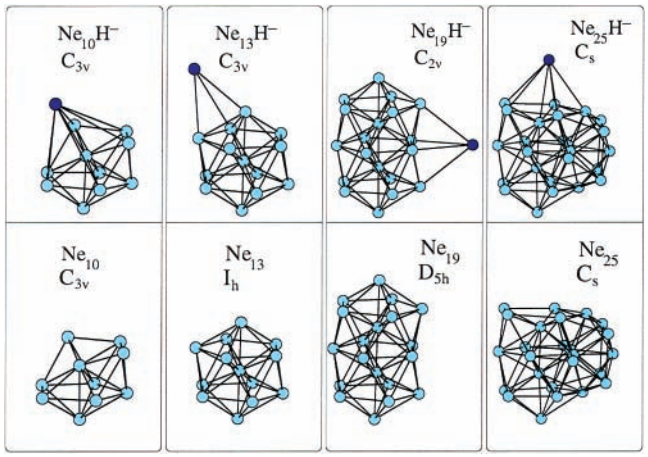

Figure 5. Optimized lowest energy structures (classical optimization method and pairwise potential model; see eqs 2 and 3) for selected Ne_nH^- and corresponding neutral Ne_n clusters.

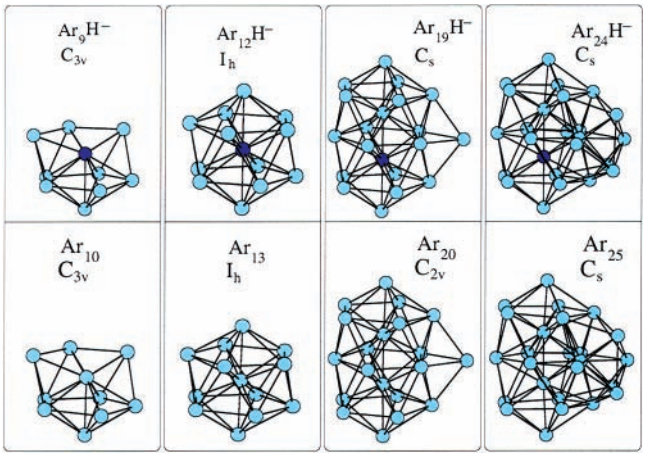

Figure 6. Optimized lowest energy structures (classical optimization method and pairwise potential model; see eqs 2 and 3) for selected Ar_nH^- and corresponding neutral Ar_{n+1} clusters.

21, which is a bicapped double icosahedron (two Rg atoms outside the Rg_{19} shell) but with a different arrangement of the two caps. This icosahedral growth feature is due to the properties of the Rg−Rg potentials, which are not sufficiently long-ranged as opposed to the Rg−H^- potentials: it is known, in fact, that only for sufficiently long-ranged potentials structures based on icosahedral packings do become energetically less favored than structures based on higher, close-packed building blocks.[51] Looking at the upper part of Figure 6, where some samples of the optimized structures of the Ar_nH^- are drawn, one can immediately see that the H^- impurity tends to replace an inner Ar atom and, as soon as the number of argon atoms is large enough, the solvation process occurs for nearly all of the structures by replacement of one inner Ar atom in the corresponding neutral cluster with the $(n + 1)$ number of particles. We therefore see that in the $Ar_{12}H^-$ cluster the first shell of argon atoms surrounding the H^- is completed, bringing out the similar icosahedral structure of the corresponding neutral counterpart Ar_{13} (second structure reported in the upper part of Figure 6): all of the Ar atoms contact the central anionic impurity, maximizing the number of Ar − H^- bonds. On the other hand, in the lowest energy structure of $Ne_{12}H^-$ (icosahedral), the impurity is located well outside the neon atoms moiety and occupies one of the two apical positions. To make a more direct and precise comparison between the geometrical features for the Ne and Ar clusters, we report in Figure 7 the moments of inertia for both the anionic and the neutral species. In the left panel of this figure, these quantities are given as functions of the number n of Ne atoms in each complex, and for the Ne_nH^- clusters, we exclude the H^- coordinates from the calculations. This means that the closer the values of the moments of inertia for both the neutral homogeneous and the doped species, the better one can view each Ne_nH^- aggregate as a Ne_n moiety with a further away H^- that does not perturb the geometrical shape of the corresponding Ne_n cluster. As pointed out before, this is what occurs for the majority of the n

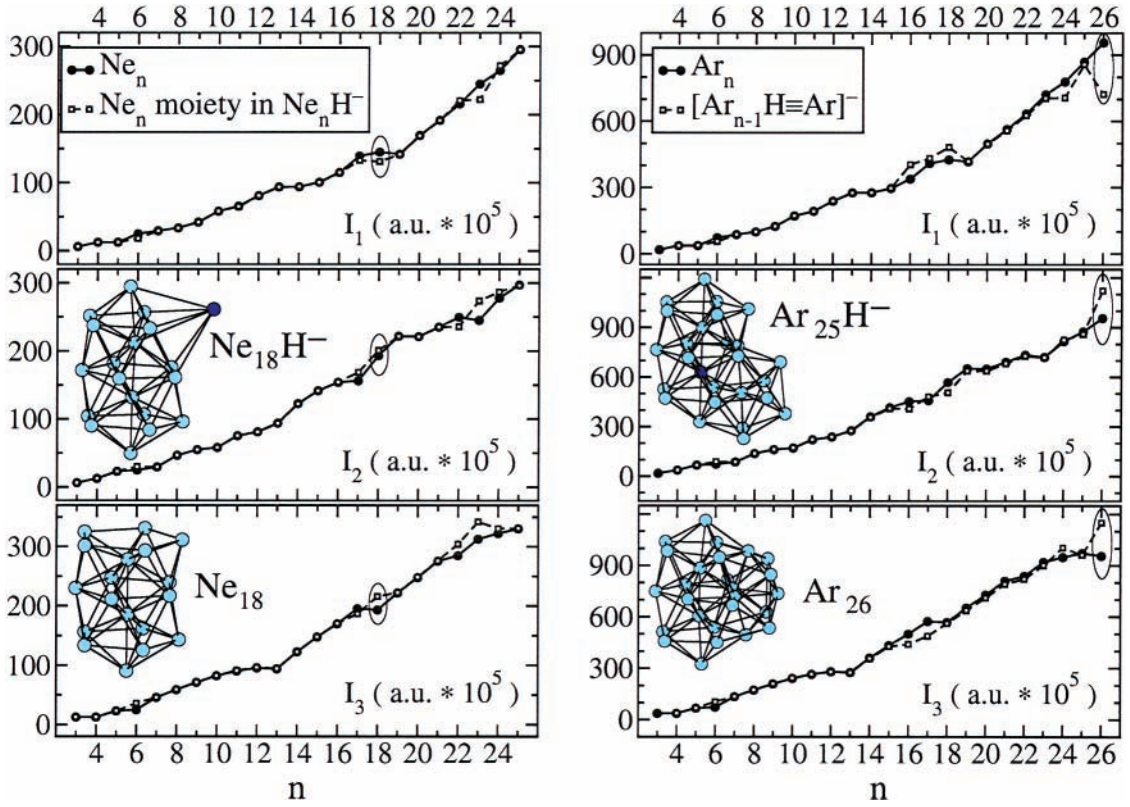

Figure 7. Left panel: the three moments of inertia (in units of $a_0 \times 10^5$) of the global minima found for the Ne_nH^- (open squares) and Ne_n (filled-in circles) clusters (using the pairwise potential model and classical optimization) are plotted as functions of the number n of Ne atoms in each complex, where for the Ne_nH^- we exclude the H^- coordinates from the calculation. Right panel: same as in left panel but for the $Ar_{n-1}H^-$ (open squares) and Ar_n (filled-in circles) clusters, where for the $Ar_{n-1}H^-$ a "fictitious mass" of argon substitutes the one of the H^- dopant. This is the meaning of "H≡Ar" in the legend. Also shown are the structures corresponding to the values marked in the two graphs.

values. The only discrepancies occur at $n = 17$, 18 and $n = 22-24$. As an example, we sketch on the left side of Figure 7 the two structures for the lowest energy geometries of $Ne_{18}H^-$ and Ne_{18}: even in this case, the arrangement of the Ne atoms in the anionic cluster differs only slightly from that in the neutral Ne_{18}. The different positioning of the H^- and one of the Ne atoms is due to the balancing effects between the shorter-ranged Ne−Ne attractive interactions and the Ne−H^- polarizability potential that remains stronger over a broader region of R values. A similar reasoning can be extended to all of the remaining couplets of structures whose values of the moments of inertia show discrepancies with respect to each other. In the right panel of Figure 7, we report the moments of inertia, as functions of the cluster size n, of the lowest energy structures that we found for the $Ar_{n-1}H^-$ and Ar_n systems. The calculation of the moments of inertia for the anionic species was done by replacing the mass of the H^- impurity with that of an Ar atom: in this way, in addition to estimating how similar the geometries of the anionic and neutral complexes are, we can check if the impurity is exactly substituting one of the Ar atoms in the structure of the neutral homogeneous aggregate with the same number of particles. The values of n for which the two sets of data mismatch correspond to the structures of the $Ar_{15}H^-$, $Ar_{16}H^-$, $Ar_{17}H^-$, $Ar_{23}H^-$, and $Ar_{25}H^-$ clusters (with respect to those of the neutral Ar_{n+1}). In the same panel, we sketch the geometries of the couplet $Ar_{25}H^-/Ar_{26}$: the H^- still occupies an Ar atom site of the double icosahedron shell of the highly symmetrical (T_d) neutral counterpart cluster, but the outer Ar atoms locate themselves in a different arrangement with respect to that in Ar_{26}, in this way experiencing more efficiently the attractive long-range (polarization) potential of the Ar−H^- interaction. A different situation occurs for the Ar_nH^- clusters

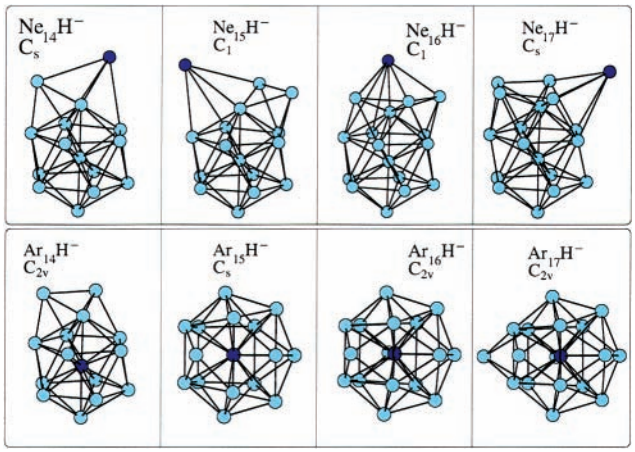

Figure 8. Optimized lowest energy structures (classical calculations and pairwise potential model; see eqs 2 and 3) for Ne_nH^- and Ar_nH^- with n from 14 to 17.

with $n = 15-17$, whose structures are reported in the lower part of Figure 8: the competition between icosahedral and close-packed geometries becomes evident. In fact, while the lowest energy minimum of $Ar_{14}H^-$ is built up as an icosahedral structure, the lowest energy minima of the remaining clusters in that figure are characterized by a close-packed growth, in this way maximizing the number of the stronger Ar−H^- bonds. For these clusters, the solvation process of the H^- impurity occurs without the substitution of one of the Ar atoms of the corresponding Ar_{n+1} lowest energy structure. Similar results were obtained by Yourshaw et al. for the Ar_nI^- clusters[28] and by Lenzer et al. for the Ar_nCl^- aggregates:[27] for the smaller impurity Cl^-, the lowest energy structures are given by the

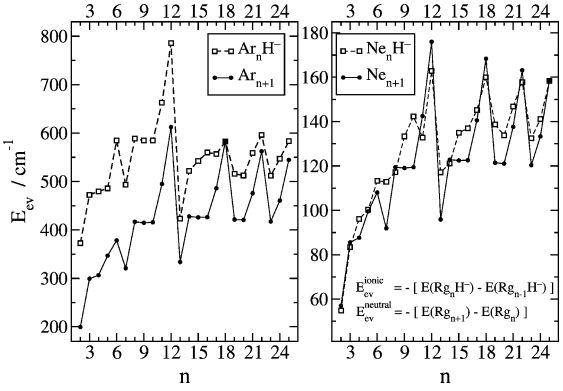

Figure 9. Left panel: single Ar atom evaporation energies (E_{ev}, calculated according to the formulas shown in the right panel) as functions of the cluster size n of all of the lowest energy structures for the Ar_nH^- (open squares) and Ar_{n+1} (filled-in circles) clusters obtained with the classical optimization. Right panel: same as in the left panel but for the Ne atom. Energies are in cm^{-1}.

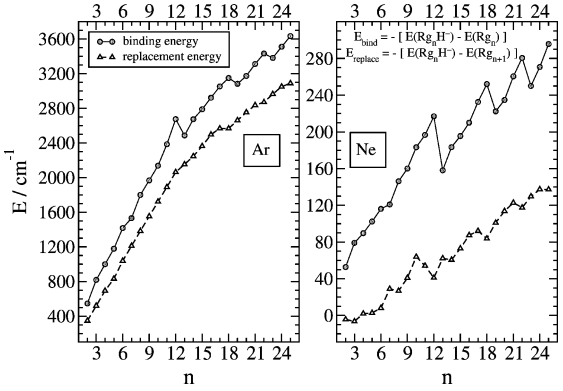

Figure 10. Left panel: Ar systems. Binding energies (shaded circles), E_{bind}, and replacement energies (open triangles), $E_{replace}$, as functions of the cluster size n, calculated according to the formulas shown in the right panel. Right panel: same as in left panel but for the Ne systems. Energies are in cm^{-1}.

icosahedral growth sequence up to $Ar_{13}Cl^-$, and for $Ar_{14}Cl^-$ and $Ar_{15}Cl^-$, the authors of ref 27 found the geometrical shapes that we have for $Ar_{14}H^-$ and $Ar_{15}H^-$. For the larger ion I^-, the minimum energy structures of Ar_nI^-, $4 \le n \le 17$, are given by close-packed configurations in which all of the Ar atoms are in direct contact with the central halide atom and even the $Ar_{12}I^-$ does not present the highly symmetrical geometry of the icosahedron. In this case, the ArI^- well depth is about four times stronger than that of Ar_2. From $Ar_{18}H^-$, the solvation with substitution of an Ar atom gives again the pattern for the growth sequence of the anionic complexes, as we can see looking back to Figures 6 and 3, where it is shown that the lowest energy cluster exhibits an icosahedral geometry and the close-packed structure just belongs to a local minimum, the crowding up of the Ar atoms around the H^- no longer allowing their positioning at about the equilibrium distance of the $Ar-H^-$ interaction potential. In the upper part of Figure 8, we report the lowest energy structures for the Ne_nH^- clusters, with $n = 14-17$, whose geometries continue to be based on the icosahedral growth sequence of the corresponding neutral Ne_n. In fact, the shape of the Ne_nH^- clusters is guided by the relative features of the Ne_2 and NeH^- curves; see Figure 1. The values of their well depths are very close, but they present different equilibrium distances so that the driving force in shaping the lowest energy geometries will be the repulsive interactions among Ne atoms.

The geometrical features and the shell solvation process can also be revealed by looking at the energetics involved with these clusters. In Figure 9, we report the single Rg atom evaporation energies E_{ev} (plotted as a function of the cluster size n and calculated via the formulas shown in the right panel) of all of the lowest energy Ar_nH^- and Ar_{n+1} clusters (left panel) and of the Ne_nH^- and Ne_{n+1} aggregates (right panel, open squares for the anionic clusters and filled-in circles for the neutral homogeneous ones). In the panels, we can note the same sequence of magic numbers[2] at $n = 12$, 18, 22, and 25 for both the Rg_nH^- and the Rg_{n+1} clusters, giving rise to the marked peaks along the curves and corresponding to particularly stable structures. For the Ar case, left panel, the two curves for the neutral and the doped species are well-separated up to $n = 12$, a separation that becomes less marked from $n = 13$: at $n = 12$, the icosahedral first shell of Ar atoms around the H^- is completed, and from this point on, the anionic clusters start to share similar features with the corresponding neutral counterparts, since the first shell of Ar atoms shields the subion. Experimental studies on Ar_nO^- carried out by means of photoelectron spectroscopy[29] are in line with our calculations. From the right panel of Figure 9, we can see that in the Ne case the values of the evaporation energy for the two systems are closer to each other and, in contrast to the Ar complexes, those of the neutral species are larger for nearly all cluster sizes. Moreover, the percentage differences between the evaporation energies of two anionic neighbor Ar and Ne clusters are, on average, fairly different; for example, for the couplet $Ar_{12}H^-/Ar_{13}H^-$, the value is about 46% while for the couplet $Ne_{12}H^-/Ne_{13}H^-$ it is only 28%. These are direct effects of the solvation process, which occurs only for the Ar_nH^- aggregates. In Figure 10, we show other quantities related to energy: the binding energy, E_{bind}, defined as

$$E_{bind} = -[E(Rg_nH^-) - E(Rg_n)], \quad (5)$$

i.e., the binding energy of H^- to the Rg_n cluster, and the replacement energy, $E_{replace}$, defined as

$$E_{replace} = -[E(Rg_nH^-) - E(Rg_{n+1})] \quad (6)$$

representing the energy released when exchanging an Ar or Ne atom with the hydride ion. Comparing the curves in the two panels, we can note how much larger the values are in the case of the Ar clusters, a feature that can be explained only by the solvation process. This is also the reason for which the E_{bind} and the $E_{replace}$ values for the Ar systems are closer to each other; for example, for $n = 12$, their percentage difference is 22.89%, while in the Ne clusters it is 81.11%.

V. Conclusions

Taking advantage of the results of refs 31 and 32, which allowed us to realistically model the global interaction forces within each H^--doped Ne and Ar cluster as a sum of pairwise potentials, and to employ the classical picture that views the cluster atoms localized at well-defined points of the configurational space, we have considered the further comparison between Ar and Ne aggregates in terms of their relative behavior with respect to the presence of an ionic dopant, the negative H^- ion. In particular, we have exploited the pairwise potential model by using Rg−Rg and Rg−H^- potential curves already tested and described earlier[31,32] and by further implementing an energy optimization[45] procedure that started from a randomly selected range of cluster geometries[31,32] and provided the global, minimum energy structures of the present clusters, both neutral and with anionic impurity. The present, detailed comparison of

the relative behavior of neon and argon clusters in the presence of the H^- adatom allows us to reach the following conclusions.

(i) The comparable strength between Ne−Ne and Ne−H^- interaction potentials (see left panel of Figure 1), but the occurrence of their energy minima locations at different distances, prevents the dopant ion from being "solvated" by the neon atom network. Thus, the H^- is always seen to attach itself on the outside of a Ne_n aggregate, which hardly differs from the same one in the neutral neon cluster sequence.

(ii) On the other hand, the larger polarizability values for the argon atom provide the key reason for the differences between potential curves and for the differences between the cluster structures that we have found in the present work. One sees, in fact, from a perusal of the data reported on the right panel of Figure 1 that the Ar−H^- well depth is much larger (about a factor of 3) than that of the neutral dimer but, at odd with the neon results, exhibits a minimum location very close to that of the Ar_2. Thus, we find that the smaller Ar_nH^-clusters immediately show the substitution of H^- for an argon atom,[32] thereby forming clusters very close in structure to Ar_{n+1} but with H^- located inside the argon aggregates.

(iii) Furthermore, as *n* increases and we move to the larger aggregates, the above molecular differences assert themselves by producing Ne_nH^- clusters, which can essentially be described as made up of undistorted Ne_n aggregates with the H^- impurity bound way outside it, while the Ar_nH^- clusters are clearly exhibiting H^- solvation. The latter, in fact, is due to the deeper well of the anionic interactions with the constituent atoms, and therefore, it causes the formation of the most stable clusters when the dopant ion penetrates inside the aggregates and replaces one of the argon atoms belonging to the core of the cluster. Thus, we can obtain the structures of Ar_nH^- clusters from that of the neutral Ar_{n+1} clusters with H^- replacing one of the inner atoms.

Acknowledgment. The financial support of the Ministry for University and Research (MIUR), of the University of Rome "La Sapienza" Research Committee, and of the INFM Institute is gratefully acknowledged. This work is dedicated to the late Gert Billing, an outstanding scientist and a dear friend, whose elegant and innovative contributions to the field of the dynamics of molecules will be always remembered.

References and Notes

(1) Roszak, S.; Leszczynski, J. *J. Phys. Chem. A* **2003**, *107*, 949−955.
(2) Solov'yov, I. A.; Solov'yov, A. V.; Greiner, W.; Koshelev, A.; Shutovich, A. *Phys. Rev. Lett.* **2003**, *90*, 053401.
(3) Castleman, A. W.; Bowen, K. H. *J. Phys. Chem.* **1996**, *100*, 12911−12944.
(4) Kalcher, J.; Sax, A. F. *Chem. Rev.* **1994**, *94*, 2291−2318.
(5) Ng, C. Y., Baer, T., Powis, I., Eds. *Cluster Ions*; John Wiley & Sons: Chichester, 1993.
(6) Smirnov, B. M. *Cluster Ions and van der Waals Molecules*; Gordon and Breach Science Publishers: Philadelphia, PA, 1992.
(7) Hiraoka, K.; Mori, T. J. *J. Chem. Phys.* **1989**, *90*, 7143−7149.
(8) Harris, I. A.; Kidwell, R. S.; Northby, J. A. *Phys. Rev. Lett.* **1984**, *53*, 2390−2393.
(9) Giju, K. T.; Roszak, S.; Leszczynski, J. *J. Chem. Phys.* **2002**, *117*, 4803−4809.
(10) Bogaerts, A. *J. Anal. At. Spectrom.* **2002**, *17*, 768−779.
(11) Lundell, J.; Pettersson, M.; Räsänen, M. *Phys. Chem. Chem. Phys.* **1999**, *1*, 4151−4155.
(12) Filippone, F.; Gianturco, F. A. *Europhys. Lett.* **1998**, *44*, 585−591.
(13) Last, I.; George, T. F. *J. Chem. Phys.* **1990**, *93*, 8925−8938.
(14) Kuntz, P. J.; Valldorf, J. *Z. Phys. D* **1988**, *8*, 195−208.
(15) Haberland, H. *Surf. Sci.* **1985**, *156*, 305−312.
(16) Soler, J. M.; Sáenz, J. J.; García, N.; Echt, O. *Chem. Phys. Lett.* **1984**, *109*, 71−75.
(17) Fieber, M.; Ding, A. M. G.; Kuntz, P. J. *Z. Phys. D* **1992**, *23*, 171−179.
(18) Naumkin, F. Y.; Wales, D. J. *Mol. Phys.* **1998**, *93*, 633−648.
(19) Gianturco, F. A.; Sebastianelli, F. *Eur. Phys. J. D* **2000**, *10*, 399−414.
(20) Sebastianelli, F.; Yurtsever, E.; Gianturco, F. A. *Int. J. Mass Spectrosc.* **2002**, *220*, 193−209.
(21) Sebastianelli, F.; Gianturco, F. A.; Yurtsever, E. *Chem. Phys.* **2003**, *290*, 279−295.
(22) Hiraoka, K.; Mori, T. *J. Chem. Phys.* **1990**, *92*, 4408−4416.
(23) Märk, T. D.; Scheier, P. *Chem. Phys. Lett.* **1987**, *137*, 245−249.
(24) Märk, T. D.; Scheier, P. *J. Chem. Phys.* **1987**, *87*, 1456−1458.
(25) Parajuli, R.; Matt, S.; Echt, O.; Stamatovic, A.; Scheier, P.; Märk, T. D. *Chem. Phys. Lett.* **2002**, *352*, 288−293.
(26) Hendricks, J. H.; de Clercq, H. L.; Freidhoff, C. B.; Arnold, S. T.; Eaton, J. G.; Fancher, C.; Lyapustina, S. A.; Snodgrass, J. T.; Bowen, K. H. *J. Chem. Phys.* **2002**, *116*, 7926−7938.
(27) Lenzer, T.; Yourshaw, I.; Furlanetto, M. R.; Pivonka, N. L.; Neumark, D. M. *J. Chem. Phys.* **2001**, *115*, 3578−3589.
(28) Yourshaw, I.; Zhao, Y.; Neumark, D. M. *J. Chem. Phys.* **1996**, *105*, 351−373.
(29) Arnold, S. T.; Hendricks, J. H.; Bowen, K. H. *J. Chem. Phys.* **1995**, *102*, 39−47.
(30) Roszak, S.; Gora, R.; Leszczynski, J. *Chem. Phys. Lett.* **1999**, *313*, 198−204.
(31) Sebastianelli, F.; Baccarelli, I.; Di Paola, C.; Gianturco, F. A. *J. Chem. Phys.* **2003**, *119*, 5570−5582.
(32) Sebastianelli, F.; Baccarelli, I.; Di Paola, C.; Gianturco, F. A. *J. Chem. Phys.* Submitted for publication.
(33) Vallet, V.; Bendazzoli, G. L.; Evangelisti, S. *Chem. Phys.* **2001**, *263*, 33−40.
(34) Tang, K. T.; Toennies, J. P. *J. Chem. Phys.* **1984**, *80*, 3726−3741.
(35) Tang, K. T.; Toennies, J. P. *J. Chem. Phys.* **2003**, *118*, 4976−4983.
(36) Slavíček, P.; Kalus, R.; Paška, P.; Odvárková, I.; Hobza, P.; Malijevsk, A. *J. Chem. Phys.* **2003**, *119*, 2102−2119.
(37) Aziz, R. A. *J. Chem. Phys.* **1993**, *99*, 4518−4525.
(38) van de Bovenkamp, J.; van Duijneveldt, F. B. *Chem. Phys. Lett.* **1999**, *309*, 287−294.
(39) Wüest, A.; Merkt, F. *J. Chem. Phys.* **2003**, *118*, 8807−8812.
(40) Kumar, A.; Meath, W. J. *Can. J. Chem.* **1985**, *63*, 1616−1630.
(41) Hotop, H.; Lineberger, W. C. *J. Phys. Chem. Ref. Data* **1975**, *4*, 539−576.
(42) Emsley, J. *The Elements*; Clarendon Press: Oxford, 1989.
(43) Chałasiński, G.; Szczęśniak, M. M. *Chem. Rev.* **2000**, *100*, 4227−4252.
(44) Frisch, M. J.; Trucks, G. W.; Schlegel, H. B.; et al. *Gaussian 98*; Gaussian, Inc.: Pittsburgh, PA, 1998.
(45) Wales, D. J. *J. Chem. Phys.* **1994**, *101*, 3750−3762.
(46) Baker, J. *J. Comput. Chem.* **1986**, *7*, 385−395.
(47) Baker, J.; Hehre, W. H. *J. Comput. Chem.* **1991**, *12*, 606−610.
(48) Naumkin, F. Y.; Wales, D. J. *Mol. Phys.* **1999**, *96*, 1295−1304.
(49) Wales, D. J.; Doye, J. P. K. *J. Phys. Chem. A* **1997**, *101*, 5111−5116.
(50) Wales, D. J.; Doye, J. P. K.; Dullweber, A.; Hodges, M. P.; Naumkin, F. Y.; Calvo, F.; Hernández-Rojas, J.; Middleton, T. F. The Cambridge Cluster Database: URL http://www-wales.ch.cam.ac.uk/CCD.html.
(51) Doye, J. P. K.; Wales, D. J.; Berry, R. S. *J. Chem. Phys.* **1995**, *103*, 4234−4249.
(52) Hoare, M. R. *Adv. Chem. Phys.* **1979**, *40*, 49−135.
(53) Mackay, A. L. *Acta Crystallogr.* **1962**, *15*, 916−918.